Separate Ways: The Mass–Metallicity Relation Does Not Strongly Correlate with Star Formation Rate in SDSS-IV MaNGA Galaxies

J. K. Barrera-Ballesteros[1], S. F. Sánchez[2], T. Heckman[1], and G. A. Blanc[3,4]
The MaNGA Team

[1] Department of Physics & Astronomy, Johns Hopkins University, Bloomberg Center, 3400 N. Charles St., Baltimore, MD 21218, USA; jbarrer3@jhu.edu
[2] Instituto de Astronomía, Universidad Nacional Autónoma de México, A.P. 70-264, 04510 México, D.F., México
[3] Observatories of the Carnegie Institution for Science, 813 Santa Barbara St, Pasadena, CA 91101, USA
[4] Departamento de Astronomía, Universidad de Chile, Camino del Observatorio 1515, Las Condes, Santiago, Chile
Received 2017 January 4; revised 2017 May 18; accepted 2017 June 18; published 2017 July 25

Abstract

We present the integrated stellar mass–metallicity relation (MZR) for more than 1700 galaxies included in the integral field area SDSS-IV MaNGA survey. The spatially resolved data allow us to determine the metallicity at the same physical scale (effective radius, R_{eff}) using a heterogeneous set of 10 abundance calibrators. In addition to scale factors, the shape of the MZR is similar for all calibrators, consistent with those reported previously using single-fiber and integral field spectroscopy. We compare the residuals of this relation against the star formation rate (SFR) and specific SFR (sSFR). We do not find a strong secondary relation of the MZR with either SFR or sSFR for any of the calibrators, in contrast with previous single-fiber spectroscopic studies. Our results agree with a scenario in which metal enrichment happens at local scales, with global outflows playing a secondary role in shaping the chemistry of galaxies and cold-gas inflows regulating the stellar formation.

Key words: galaxies: evolution – galaxies: fundamental parameters – ISM: abundances – techniques: imaging spectroscopy

1. Introduction

Current chemical content in nearby galaxies is the consequence of the star formation and chemical enrichment histories. In particular, the observed oxygen abundance is a consequence of cosmological evolution. As result, these abundances present strong correlations with other parameters such as the total stellar mass.

Although the relation between the galaxy luminosity and metallicity has been known for decades (e.g., Vila-Costas & Edmunds 1992), the mass–metallicity relation (MZR) was introduced by Tremonti et al. (2004). It exhibits a tight correlation between the integrated stellar mass and the average oxygen abundance of galaxies: as stellar mass increases, the metallicity increases, reaching a saturation at high stellar masses. They derived the MZR with a tight dispersion (∼0.1 dex) for ∼40,000 galaxies extracted from the SDSS spectroscopic sample at $z \sim 0.1$. Although its functional form seems to depend on the adopted abundance calibrator (e.g., Kewley & Ellison 2008), it is rather stable when using single aperture spectroscopic data or spatial resolved information (e.g., Rosales-Ortega et al. 2012; Sánchez et al. 2014).

The MZR was interpreted by Tremonti et al. (2004) as the result of galactic outflows regulating the metal content of the interstellar medium. Alternatively, Rosales-Ortega et al. (2012) showed that the integrated relation is easily derived from a new, more fundamental relation between the stellar mass density and the local oxygen abundance. This relation has been previously confirmed by Sánchez et al. (2013) and recently using MaNGA data by Barrera-Ballesteros et al. (2016). In this scenario the stellar mass growth and the metal enrichment are both dominated by local processes, in situ star formation, with a little influence from outflows or radial migrations.

Different authors have investigated a possible dependence of the MZR on the star formation rate (SFR; e.g., Ellison et al. 2008; Lara-López et al. 2010; Mannucci et al. 2010; Telford et al. 2016). In different degrees, these studies show that at a fixed stellar mass, galaxies with stronger SFRs exhibit lower oxygen abundances. Although the adopted functional form for this secondary relation is different depending on the study, the conclusions are similar. Since oxygen abundance is enhanced due to star formation, which in turn is directly related to the production of SN II, the proposed secondary correlation is therefore not quite intuitive. These studies are based on subsamples of the same observational data set, the SDSS spectroscopic survey at $z \sim 0.1$. Despite the application of aperture corrections (Brinchmann et al. 2004), the spectroscopic information is affected by strong aperture effects (e.g., Iglesias-Páramo et al. 2013, 2016; Gomes et al. 2016).

Sánchez et al. (2013) could not confirm this secondary relation using integral field spectroscopic data covering the full optical extension of the galaxies, extracted from the CALIFA data set (Sánchez et al. 2012). This result was confirmed recently with more statistics by Sánchez et al. (2015a). In a study using drift-scan integrated spectra, Hughes et al. (2013) showed that a secondary relation of the MZR with the SFR is not present. Indeed, Rosales-Ortega et al. (2012) had already shown that the relation with the specific SFR (sSFR; using the Hα equivalent width [EW(Hα)] as a proxy) of the local MZ relation does not present a secondary trend, but follows the primary relation between the SFR and stellar mass, as studied in detail by Sánchez et al. (2013) and more recently by Cano-Díaz et al. (2016). These results were also discussed in Salim et al. (2014), who divided the data presented by Sánchez et al. (2013) in mass bins and found a correlation between the metallicity and the sSFR in each of those bins. Those correlations are easily explained as a consequence of the

combination between the SFR mass and MZRs. These secondary dependences disappear if the primary dependence of the mass with metallicity is removed. Finally, Moran et al. (2012) showed that this secondary relation is not shown in their data; rather, they propose a secondary relation with the gas fraction. Thus, the secondary relation of the SFR and the MZR has been observed, so far, only in aperture-based spectroscopic observations.

In this article we explore the MZR and its possible dependence with the SFRs and sSFRs for more than 1700 galaxies included in the spatially resolved spectroscopic MaNGA survey (Bundy et al. 2015). The article is organized as follows. In Section 2 we present our sample of galaxies, an overview of the data set, and a brief description of the 10 calibrators used to derive the oxygen abundance. The statistical wealth of data allows us to present, in Section 3, the MZR at the same physical scale (i.e., $R_{\rm eff}$). We explore the possible dependence of its residuals on the SFR and sSFR in Section 4, as well as the impact of the stellar mass and aperture effects in these residuals; these results are discussed in Section 5. Finally, we present our main conclusions in Section 6.

2. Sample and Data

2.1. The MaNGA Sample

For this study we use the observed sample by the MaNGA survey until 2016 June (2730 galaxies at redshift $0.03 < z < 0.17$). The goal of the ongoing MaNGA survey is to observe approximately 10.000 targets; detailed description of the selection parameters can be found in Bundy et al. (2015) and a description of the sample properties can be found in Wake (2016). The MaNGA survey takes place at the 2.5 m Apache Point Observatory (Gunn et al. 2006). Observations are carried out using a set of 17 different fiber-bundles science Integral Field Units (IFUs) (Drory et al. 2015). These IFUs feed two dual-channel spectrographs (Smee et al. 2013). Details of the survey spectrophotometric calibrations can be found in Yan et al. (2016). Observed datacubes are reduced by a dedicated pipeline described in Law et al. (2016). This sample covers a wide range of parameters (e.g., stellar mass, SFR and morphology), providing a unique view of galactic properties in the Local universe.

To extract the two-dimensional physical properties from the reduced datacubes, we used the analysis pipeline PIPE3D (Sánchez et al. 2016). For a detailed description of the fitting procedure and uncertainty determination, see Sánchez et al. (2015b). An overview on how this pipeline extracts the maps of the physical properties from ionized-gas emission-line data-cubes is described in Barrera-Ballesteros et al. (2016). Prior to deriving the characteristic oxygen abundances in each galaxy, we first select those regions (i.e., spaxels) that meet the following criteria: (a) flux ratios ([O III]/Hβ and [N II]/Hα) lying in the star-forming region of a BPT (Baldwin et al. 1981) diagnostic diagram (i.e., below the Kauffmann et al. (2003) demarcation line) and (b) an EW(Hα) larger than 6 Å. These combined criteria ensure that the ionization is due to young stars (e.g., Cid Fernandes et al. 2011; Sánchez et al. 2014). We convert the luminosity of the Hα emission line for each of the spaxels to their SFR using the relation presented in Kennicutt (1998). Then, we co-add it through those spaxels with an ionization compatible with star formation to derive the integrated SFR. The result of obtaining the total SFR using
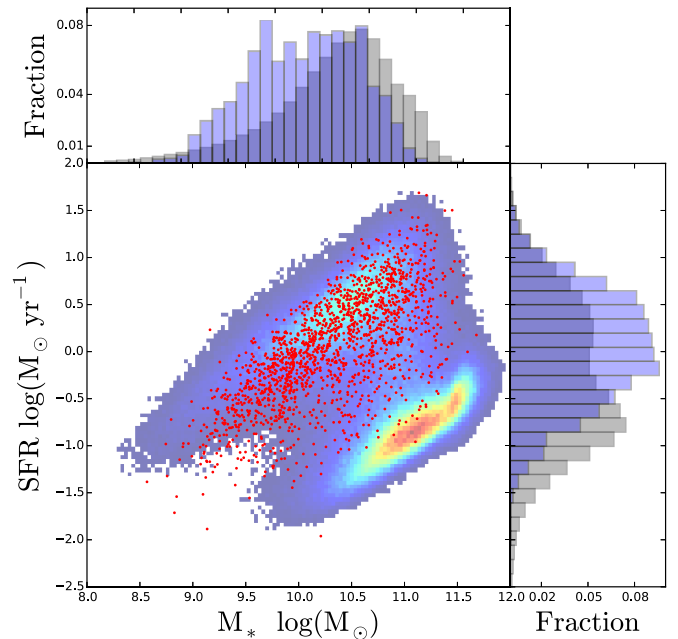
Figure 1. Comparison of our sample of galaxies and the SDSS-DR7 sample in the stellar mass–SFR plane. The background distribution shows the well-known star formation and retired sequence in the SDSS galaxies. The red points show the total SFR and stellar masses for our selected sample (1704 galaxies). On the horizontal and vertical histograms we compare the stellar mass and SFR distributions for these two samples. In these histograms, the gray and blue panels represent the SDSS and our sample, respectively.

this procedure does not change substantially from typical methods; for instance, consider the total SFR from the integrated Hα flux within the IFU's field of view (e.g., Catalán-Torrecilla et al. 2015).

In addition, we determine the oxygen abundance for each spaxel using the different calibrators presented in Section 2.2. The oxygen abundances presented in this article are determined as those at the effective radius $R_{\rm eff}$ from the best-fit gradient in each calibrator. Details regarding the method used to derive the abundance gradient are described in Sánchez et al. (2013) and Sánchez-Menguiano et al. (2016). The photometric properties of the galaxies (stellar mass [$M_\odot$], major position angle, and ellipticity) are obtained from the NSA catalog.[5] As a final sample we use those galaxies where it is possible to determine the oxygen abundance at the $R_{\rm eff}$ that fulfill the above criteria (i.e., 1704 objects). This selected sample corresponds mainly to galaxies located in the star-forming main-sequence in the stellar mass–SFR plane (see Figure 1).

2.2. Abundance Calibrators

In order to analyze possible discrepancies between different abundance calibrator derivations and to explore the MZR in the most general way, we adopted a heterogeneous set of 10 abundance calibrators. We derive the abundance using (i) calibrators based on the "direct-method," including the O3N2 and N2 line-ratio calibrators proposed by Marino et al. (2013; hereafter O3N2-M13 and N2, respectively), the calibration described in Rosales-Ortega (2010; hereafter R23), and the calibrator proposed by Pilyugin et al. (2010, hereafter ONS); (ii) an electronic-temperature-corrected calibrator proposed by Peña-Guerrero et al. (2012) for an average of the

---
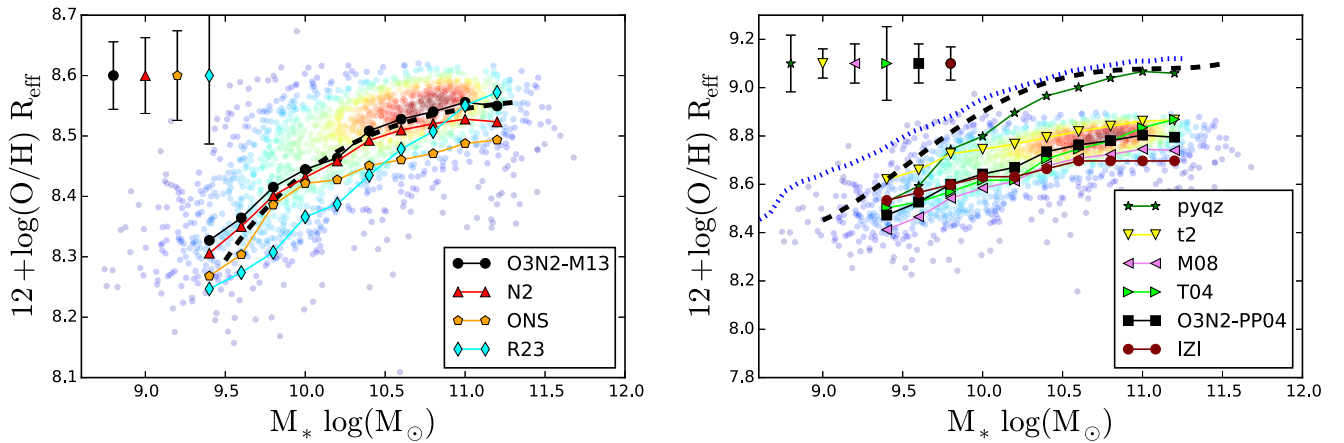
Figure 2. MZR using different metallicity calibrators measured at $R_{\rm eff}$ for more than 1700 MaNGA galaxies. Line-connected symbols represent median values at a given mass bin for the different calibrators. The error bars in the top left corners represent the average standard deviations for each indicator at different mass bins. In the left panel we use direct-method-based metallicity calibrators (see Section 2.2 for their references); O3N2-M13, black dots; N2, red triangles; ONS, orange pentagons; and R23, cyan diamonds. For the references of the dynamical range, we plot in the background the MZR for individual galaxies color-coded by their densities using the O3N2-M13 calibrator. The dashed curve represents the best fit of the MZR derived for the CALIFA sample (Sánchez et al. 2014). In the right panel we use semi-empirical or modeled calibrators (O3N2-P04, blue squares; pyqz, green stars; t2, yellow down-triangles; M08, left-triangles; T04, right-triangles; IZI, maroon filled-circles). Similar to the left panel, we plot the individual values for all the sample using the O3N2-P04 indicator. The black dashed curve represents the best fit from Mannucci et al. (2010). The dotted blue curve represents the median values from Tremonti et al. (2004).

Table 1
Fitting Parameters for the MZR and Its Scatter for the Set of Abundance Calibrators Used in This Study

Metallicity Indicator	MZ Best Fit		σ MZ scatter (dex)	ΔMZ Best Fit		$\sigma\Delta$ MZ Scatter (dex)
	a (dex)	b (dex / $\log(M_\odot)$)		α (dex)	β (dex/$\log(M_\odot\,{\rm yr}^{-1})$)	
O3N2-M13	8.56 ± 0.02	0.005 ± 0.013	0.067	-0.005 ± 0.1	0.001 ± 0.002	0.067
N2	8.53 ± 0.01	0.01 ± 0.01	0.069	-0.016 ± 0.02	-0.013 ± 0.002	0.067
ONS	8.49 ± 0.02	0.01 ± 0.02	0.075	-0.027 ± 0.01	-0.003 ± 0.001	0.075
R23	8.53 ± 0.09	0.006 ± 0.052	0.125	-0.053 ± 0.031	-0.006 ± 0.003	0.125
O3N2-P04	8.82 ± 0.03	0.007 ± 0.020	0.097	0.047 ± 0.039	0.007 ± 0.004	0.098
pyqz	9.10 ± 0.05	0.013 ± 0.030	0.137	-0.061 ± 0.021	-0.006 ± 0.002	0.138
t2	8.87 ± 0.03	0.005 ± 0.017	0.073	-0.030 ± 0.048	-0.003 ± 0.006	0.073
M08	8.76 ± 0.03	0.007 ± 0.019	0.097	-0.048 ± 0.018	-0.005 ± 0.002	0.097
T04	8.79 ± 0.13	0.006 ± 0.064	0.167	0.006 ± 0.006	0.001 ± 0.002	0.167
IZI	8.71 ± 0.02	0.005 ± 0.019	0.059	0.008 ± 0.027	0.001 ± 0.003	0.059

Note. For each calibrator we list the parameters a and b from the fitting of Equation (1) to the MZR; the $\sigma\Delta$ MZ scatter lists the standard deviation of the residuals after subtracting the best fit to the MZR; the parameters α and β represent the linear fitting of the residuals of the MZR with respect to the SFR (see Section 4); the $\sigma\Delta$ MZ scatter lists the standard deviation of the scatter of the linear fitting using the above parameters.

abundances derived using the four previous methods (hereafter t_2); (iii) two mixed calibrators based on the O3N2 calibrator (Pettini & Pagel 2004, hereafter O3N2-PP04) and the R23 indicator (Maiolino et al. 2008, hereafter M08); (iv) two calibrators based on pure photoionization models, particularly the one included in the pyqz code, which makes use of the O2, N2, S2, O3O2, O3N2, N2S2, and O3S2 line ratios as described in Dopita et al. (2013, hereafter pyqz) and the one adopted by Tremonti et al. (2004) in their exploration of the MZR based on the R23 line ratio (hereafter T04); and finally (v), a code to infer the metallicity from strong emission lines using Bayesian statistics (Blanc et al. 2015, hereafter, IZI).

3. The MaNGA Integrated MZ Relation

In Figure 2 we present the MZR for our sample of MaNGA targets using the 10 different calibrators listed in the first column of Table 1. For visualization purposes, we plot the average metallicity at different stellar mass bins for our set of calibrators in two different panels. The left panel shows the MZR derived using only direct-method calibrators, whereas the right panel shows mixed and photoionization-model-based calibrators.

As we explained in Section 2.2, the derivation of these calibrators is quite heterogeneous. However, it is remarkable that metallicities derived from these different calibrators follow a similar trend. Metallicity increases with stellar mass, reaching a constant value for more massive galaxies. Depending on the indicator, the absolute scale of the relation varies. For comparison, in the left panel of Figure 2 we plot the best-fit curve of the MZR derived from the CALIFA survey (see the dashed black curve, Sánchez et al. 2014). This curve is in excellent agreement with the MZR derived using direct-method calibrators. We also plot in the right panel of Figure 2 the best-fitted curve of the MZR derived by Mannucci et al. (2010) and the median values from Tremonti et al. (2004; see their Table 3) using single-fiber spectroscopic data (see black dashed and blue dotted curves in the left panel of Figure 2, respectively). The curve derived by Mannucci et al. (2010) shows very good agreement with the median points from the pyqz calibrator (green

points). On the other hand, the curve from Tremonti et al. (2004) shows an offset at higher metallicities for low-mass galaxies.

## 4. The SFR and sSFR Dependence of the MZR Residuals

In order to determine the residuals of the MZR for each indicator, we fit their median values at different mass bins using the functional form between these two parameters introduced by Moustakas et al. (2011) and used by Sánchez et al. (2013):

$$y = a + b(x - c)\exp(-(x - c)), \tag{1}$$

where $y = 12 + \log(O/H)$ and $x = \log(M_*/M_\odot) - 8.0$. This functional form has been motivated by the shape of the MZR (Sánchez et al. 2013). The fitting coefficients a, b, and c represent the maximum metallicity, the curvature of the line, and the stellar mass where the metallicity reaches its maximum, respectively. We fix to $c = 4.0$ since at that mass the abundance is almost constant for any calibrator. In Table 1 we present the best-fitted parameters a and b for all the calibrators. As expected from Figure 2, direct-method based calibrators show low values of a. The b coefficient does not depend strongly on the calibrator, in fact, within their uncertainties they are all similar.

We obtain the residuals of the MZR ($\Delta \log(O/H)$) for each calibrator by subtracting the metallicities from the best-fit curve. The standard deviation for each of them (σ MZ scatter) is listed in Table 1 (see also the error bars in Figure 3). We find that the direct-method, t2 -based, and `IZI`-Bayesian-based calibrators show lower dispersion in their scatter (~0.06–0.07 dex) compared to model-based or mixed calibrators (~0.10–0.16 dex). This difference in the scatter of the MZR suggests that hybrid or model-based calibrators may introduce an artificial higher dynamical range of the residuals in comparison to the direct-method and t2 calibrators. We also perform a similar analysis using a grade-forth polynomial as a fitting function, following Mannucci et al. (2010). We found similar standard deviations in the scatter as those reported in Table 1.

To explore the possible secondary dependence of the MZR on the SFR, it is necessary to study whether the residuals of the primary relation correlated with the SFR. In Figure 3 we plot for each calibrator the median value of the $\Delta \log(O/H)$ within bins of SFR of $0.3 \log(M_\odot \, yr^{-1})$ width in a range of -1.5 and $1.0 \log(M_\odot \, yr^{-1})$. We find a good agreement for these medians for all the calibrators. Furthermore, the dynamical range of these medians is smaller than ± 0.1 dex, which is the typical deviation of the MZR scatter. In other words, from these comparisons we do not find a significant trend for the scatter of the metallicity with respect to the SFR, except for a very mild decrement of the residuals at low SFR, for some calibrators (e.g., N2, R23, and t2). Nevertheless, to quantify the possible linear relation of the scatter (i.e., a secondary relation of the SFR with respect to the MZR), we perform a linear fitting of these two parameters for our set of calibrators. In Table 1 we listed the best-fitted parameters (α and β for the zero-point and slope, respectively) for all the calibrators. We found that both the slope (α) and the zero-point (β) are nearly zero. This is further evidence that there is not a secondary relation of the MZR with the SFR. We also note that the standard deviation of the residuals of this linear fitting is similar to the one derived from the MZR fitting (see the last column in Table 1).
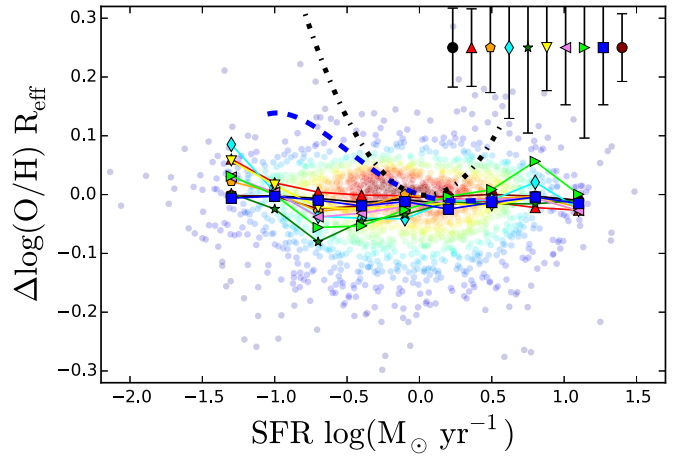
Figure 3. MZR residuals from their best-fitting curve against the SFR using different abundance indicators. The plots connected by lines represent median values at a given SFR bin. The error bars in the top corner represent, for each indicator, the dispersion of the residuals from the best linear fit (see the details in Section 4). For each calibrator we use the same symbols as in Figure 2. For comparison we plot in the background the distribution of these residuals using the O3N2-M13 calibrator. The dashed line represents the relation between the scatter and the SFR presented in Mannucci et al. (2010), while the dotted line represents the relation from Lara-López et al. (2010).

In Figure 3 we compare two secondary relations reported in the literature with $\Delta \log(O/H)$ (Lara-López et al. 2010; Mannucci et al. 2010, blue dashed and black dotted lines, respectively). As prescribed by Mannucci et al. (2010), we build the blue dashed curve by subtracting their relation without SFR dependence (i.e., μ_0 in their Equation (4) from the same relation with SFR dependence (i.e., $\mu_{0.32}$). Similarly, we build the black dotted curve by subtracting from the MZ–SFR relation with the curve obtained by removing the effect of the SFR in Equation (1) in Lara-López et al. (2010). The relation presented by Mannucci et al. (2010) highlights the fact that the secondary relation of the SFR is more evident at low stellar masses (see their Figure 1), as observed in our plot (see the blue dashed line in Figure 3). Although it is evident that there is a disagreement at low SFRs between this curve and our results, at larger SFRs this curve is a good representation of the scatter for almost all the calibrators. In any case, this would happen if there was no dependence with the SFR at all. On the other hand, we do not find any correspondence between our data and the possible secondary relation of the SFR with the MZR described by the dotted black line in Figure 3 from Lara-López et al. (2010) at any SFR range, except at SFR $\sim 1.0 \, M_\odot \, yr^{-1}$. In the next section we explore whether the presence of a relation of the SFR and $\Delta \log(O/H)$ can be observed at different stellar mass bins.

Finally, in Figure 4 we compare the residuals of the MZR with the sSFR. Except at the lowest bin of sSFR, we find that residuals do not vary significantly as a function of the sSFR, regardless of the abundance calibrator. This trend has also been observed in single-fiber spectroscopic studies. Tremonti et al. (2004) noted that the residuals of their derived MZR do not depend on the EW(Hα), which is a direct proxy for sSFR (see bottom-right panel in their Figure 7). For the lowest bin of sSFR the median metallicity residuals change drastically depending on the calibrator. Some of them show a positive residual (e.g., T04), a zero residual (e.g., T04), or negative residuals (e.g., pyqz).
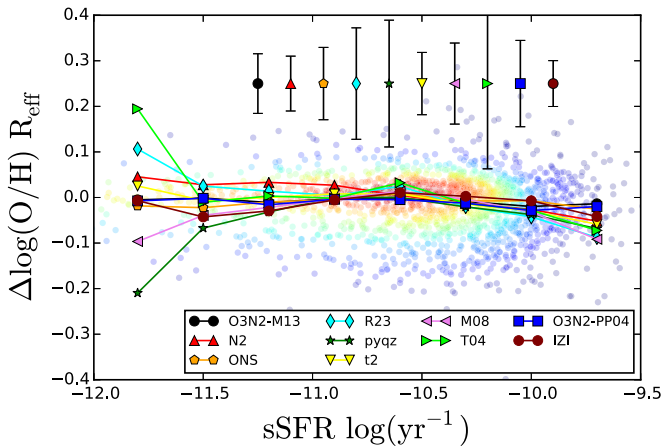
Figure 4. MZR residuals from their best-fitting curve as a function of the sSFR. The plots connected by lines represent median values at a given sSFR bin. The error bars at the bottom of the figure represent the dispersion of the residuals from the best linear fit. For each calibrator we use the same symbols as in Figure 2.

4.1. Impact of Stellar Mass in the MZR Residuals

The large sample of MaNGA galaxies allows us to further investigate the possible interplay between stellar mass and star formation with regard to metallicity. Even though we remove the stellar mass dependence in the metallicity by studying the residuals of the MZR, we still can ask how their observed relation (or lack thereof) with the SFR changes for different stellar masses. In Figure 5 we plot $\Delta \log(O/H)$ against the SFR for three different mass bins from left to right: low, intermediate, and high stellar mass galaxies. For the low-mass bin, the residuals of the MZR seems to decrease with the SFR $< 1.0 \, M_\odot \, \mathrm{yr}^{-1}$. For larger SFRs, the trend is not clear: some calibrators show larger residuals, whereas the O3N2-based calibrators show residuals close to zero. In the low-mass bin for the range of SFRs where we observe the decrement in the residuals, we note that for a given SFR these residuals are smaller than the reported trend in Mannucci et al. (2010). In fact, in log scale the slopes of the trends for all the calibrators are smaller than the slope presented in Mannucci et al. (2010) (0.03 to 0.23 dex/$M_\odot \, \mathrm{yr}^{-1}$). Furthermore, the standard deviation of the residual distributions at low SFR bins is consistent with $\Delta \log(O/H) = 0$ dex. The scarce fraction of galaxies with measured metallicities at high SFRs in this low-mass bin may explain the abrupt difference in the residuals at high SFRs.

For the intermediate-mass bin, the trends for the different calibrators are mixed. Some calibrators seem to decrease as the SFR increases (e.g., R23 and T04), while others show a constant trend around zero scatter (e.g., O3N2, ONS, and IZI). As we mentioned above, most of the calibrators are not available for high SFRs, which may induce the strong decrement at high SFRs. Without considering that last SFR bin, the distributions of all the calibrators are, within their deviations, consistent with a constant zero residual. As for the low-mass bin, the residual distributions at low SFRs are smaller than those reported in Mannucci et al. (2010), except for the R23, pyqz, and T04 calibrators; the deviations of their distributions are larger than the blue line.

For the most massive galaxies (right panel in Figure 5), in most of the calibrators (except pyqz) the median residuals are rather constant around $\Delta \log(O/H) \sim 0$ dex for the different SFR bins. For the calibrators with the largest deviations (i.e., N2, ONS,

and R23), the residual distributions include the trend depicted by the blue dashed line, making it statistically inconclusive whether or not the trend presented in Mannucci et al. (2010) can be described using these calibrators.

In Figure 6 we study the residuals of the MZR with the sSFRs at different stellar mass bins. For the low-mass bin (left panel of Figure 6), the observed trend of the residuals with the sSFRs depends strongly on the calibrator. Some calibrators show a significant decrease in the residual with sSFR (e.g., N2), whereas others do not exhibit an evident trend in the residuals with the SFR (e.g., O3N2-M13). A linear fitting of these two parameters quantifies these trends from negative slopes to no trend (-0.17 to 0.001 dex / $\log(\mathrm{yr}^{-1})$). As we note above, for the relation of between MZR residuals and SFR, the large distributions of the residuals at different bins of sSFR also make the observed negative trends compatible with the MZR residuals showing no trend with the sSFR. For the intermediate stellar masses (middle panel in Figure 6), all the calibrators seem to show no relation between the residuals and the sSFR. For the most massive galaxies within the error bars the residuals show a lack of a trend with the SFR. This further exploration of the MZR residual at different stellar masses suggests that our results in Figures 3 and 4 appear to be independent on the considered mass range. In other words, metallicity does not strongly depend on the SFR.

4.2. Central MaNGA Metallicities

Spatially resolved observations allow us to measure physical properties at different galactic scales. Above, we analyzed the metallicities derived at the effective radius using the fitting of the radial metallicity gradient. Nevertheless, we can select any aperture or region within the area covered by the field of view of the IFU instrument. One particular region of interest is the central 3 arcsec area of the observed galaxies. This is the same area covered by the single-fiber aperture from SDSS spectroscopic data. We perform the same analysis as in Section 3 using the necessary fluxes to determine the metallicity from a 3 arcsec aperture centered in the optical nucleus of our sample of galaxies. Although not shown here, the MZR using the metallicity from this 3 arcsec aperture is very similar to the one observed in Section 2 for all the calibrators. Once we obtain the residuals of the MZR from the best fit using Equation (1), we proceed to compare these residuals with the SFR and sSFR following the same strategy as above. In Figures 7 and 8 we plot the same results as in Figures 3 and 4, but instead use the residuals of the MZR from the central 3 arcsec aperture.

Comparing these residuals to those derived at the effective radius, we find that they show a slightly larger scatter among the different calibrators than the values derived at the effective radius when compared to the SFR (see Figure 7). This indicates that metallicity measurements at R_{eff} are better for characterizing the entire galaxy's metallicity (e.g., Sánchez et al. 2014, 2017). Similar to the effective radius measurements, there are some calibrators that exhibit a very mild decrement of the MZR residuals as the SFR increases (e.g., N2, R23, and t2). In any case, the residuals from all the calibrators tend to have zero residuals at large SFR values. As for the metallicities measured at the effective radius, despite the mild decrement of these residuals at low SFR values, these median residuals are consistently lower than the values expected from the relations
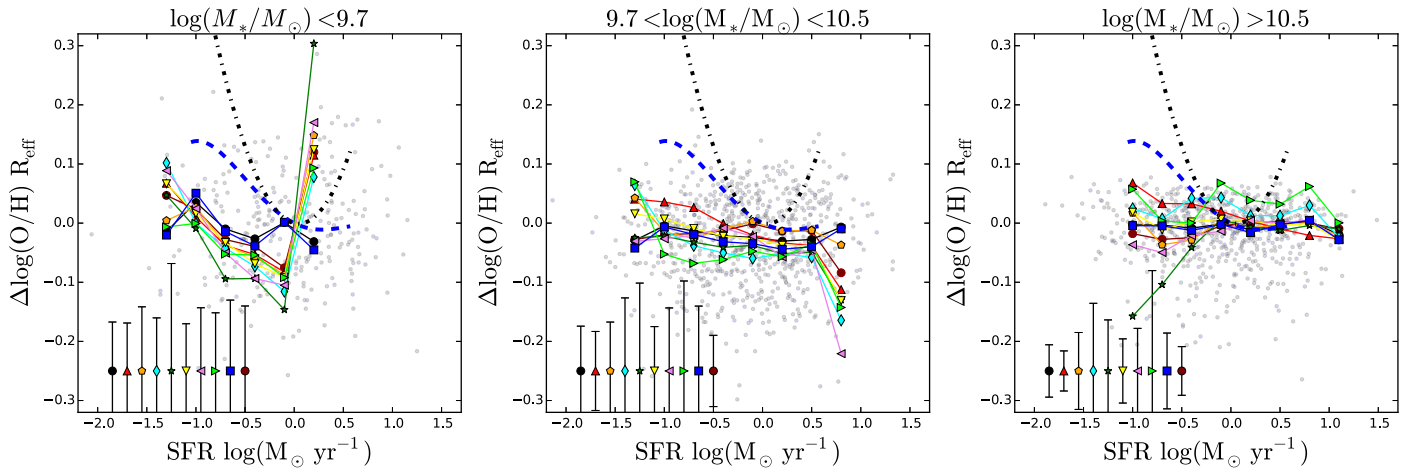
Figure 5. MZR residuals from their best-fitting curve as a function of the SFRs for different stellar mass bins. The sample has been binned in three stellar masses: low, intermediate, and high (left, middle, and right panels, respectively). The color-coding for the lines, symbols, and error bars are the same as in Figure 3. The data points represent the residuals from the O3N2-M13 calibrator.

presented by Mannucci et al. (2010) and Lara-López et al. (2010).

On the other hand, the trend from these same metallicity residuals against the sSFR differs considerably in comparison with those derived at R_{eff}. Some calibrators show a clear trend, with residuals increasing as the sSFR decreases (T04, ONS, R23, and N2), whereas others remain constant at different sSFRs (O3N2-M13, O3N2-PP04, IZI, M08, and IZI). In summary, these results suggest that even when we consider the metallicity in a central 3 arcsec aperture, there seems to be no clear relation between the residuals and the SFR, even at low SFR regimes, for any of the metallicity calibrators used in this study. On the other hand, for the sSFRs there seems to be some increment of the residuals at low sSFRs at this particular aperture. However, as we have seen above, it depends strongly on the calibrator.

5. Discussion

The main goal of this article is to shed some light on the question of whether or not there is a secondary relation in the already tight stellar MZR at global scales. With this idea in mind, we constructed the MZR from a heterogeneous set of 10 metallicity calibrators. Thanks to the spatially resolved data provided by the MaNGA survey, all our metallicity measurements are derived at the effective radius of our sampled galaxies. In Figure 2 we presented the MZR for the set of calibrators. As we noted in Section 3, apart from scaling factors, the trend observed for all the calibrators is similar; as the stellar mass increases the metallicity increases, reaching a constant plateau. This remarkable result shows the robustness of the MZR regardless of the metallicity calibrator when measured at the effective radius. Using this result we explore the possible secondary relation of the (s)SFR with the metallicity residuals from the best-fit relation of the MZR for each calibrator. As proposed by Mannucci et al. (2010) and Lara-López et al. (2010), if there is a secondary relation of the (s)SFR with the MZR, one may expect a reduction in the scatter of the MZR when the SFR is introduced as a second parameter. In other words, if there is a secondary relation we should observe a clear trend between the residuals and the (s)SFR. Since the MZR shape appears to be generally independent of the calibrator, we should expect that this possible trend

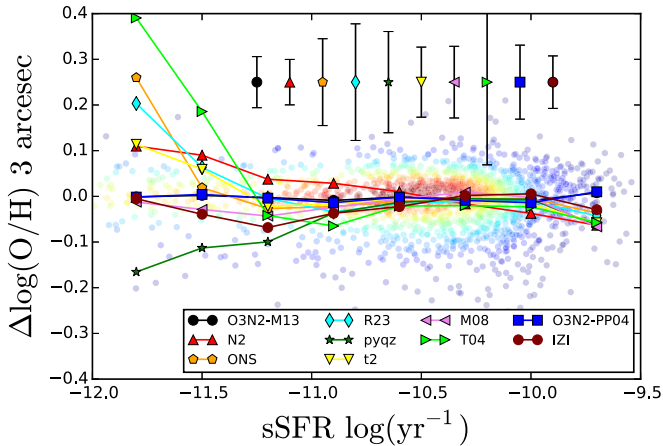between the above parameters is also independent of the calibrator.

In Figures 3 and 4, respectively, we show comparisons of the MZR residuals against the SFRs and sSFRs for the set of 10 calibrators. In Figure 3 the discontinuous dotted and dashed lines represent two relations derived using single-fiber spectroscopy from the SDSS survey by Lara-López et al. (2010) and Mannucci et al. (2010), respectively. On the one hand, Lara-López et al. (2010) assumes that these three observables lie in a so-called "fundamental plane." In other words, each of these observables can be described as a liner combination of the other two. These authors claim that for their observed parameters, this plane reduced the scatter from ~ 0.26 as observed in their MZR to ~ 0.16 dex as observed in the plane. The expected relation is very steep, decreasing more than 0.3 dex from SFR from 0.1 to 1 $M_{\odot}$ yr^{-1}. When we compare their expected metallicity residuals from this plane against the SFR with our observed residual, we are not able to reproduce them with any of the MZR residuals from our set of metallicity calibrators. Alternatively, Mannucci et al. (2010) parameterized the metallicity as a function of a new parameter [$\mu_{\alpha} = \log(M_*/M_{\odot}) + \alpha \log(SFR)$]. These authors showed that $\alpha = -0.32$ provides the best fit to their data. This in turn suggests that low-mass galaxies with low star formation rates tend to have high metallicities. Following this relation we should expect larger metallicity residuals in galaxies with low SFRs than those with high SFRs, as represented by the blue dashed line in Figure 3. For these authors, the MZR residuals decrease from ~ 0.15 to 0.0 dex in a small SFR range (from 0.1 to 1 $M_{\odot}$ yr^{-1}). In contrast, we do not observed this trend with the same amplitude in the median MZR residuals from our set of calibrators. However, for some of these calibrators there seems to be a trend of decreasing MZR residuals with the SFR (e.g., R23, N2, and t2). It may be the case that due to the statistical coverage, we are not able to sufficiently sample the trend presented by Mannucci et al. (2010) at low SFR. In order to explore this, we compare in Figure 9 the residuals of the calibrator with the tightest MZR relation (i.e., t2) along with one of the calibrators with almost zero MZR residual variations with respect to the SFR (i.e., O3N2-M13). The yellow and gray shaded regions represent the standard deviation of the residuals covered by each of these calibrators at different SFR bins. For
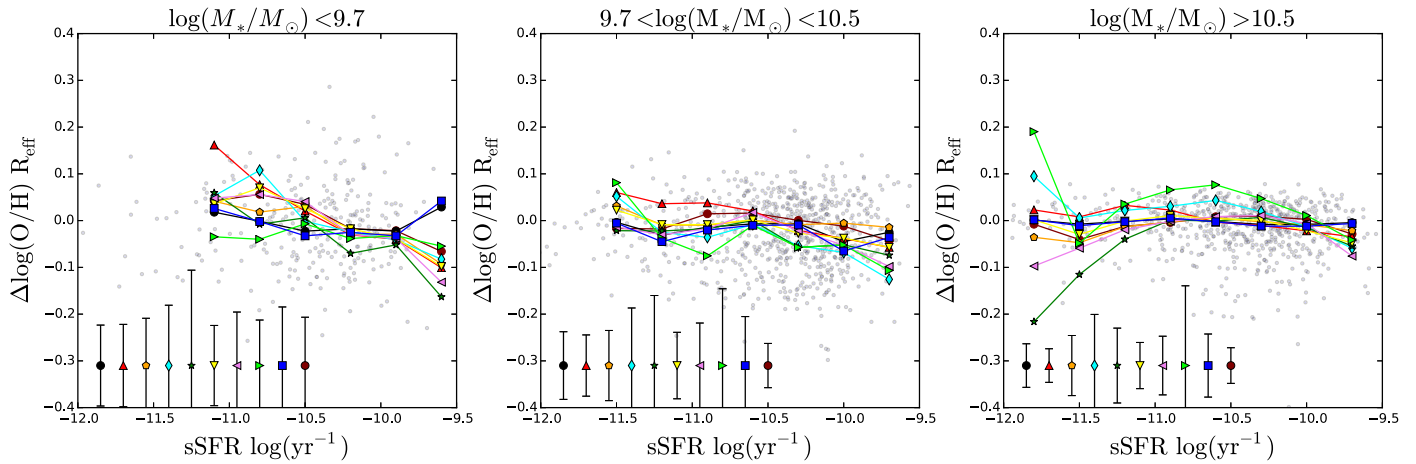
Figure 6. MZR residuals from their best-fitting curves as a function of the sSFRs for different stellar mass bins. The stellar mass bins are the same as in Figure 5. The color-coding for the lines, symbols and error bars are the same as in Figure 4. The data points represent the residuals from the O3N2-M13 calibrator.
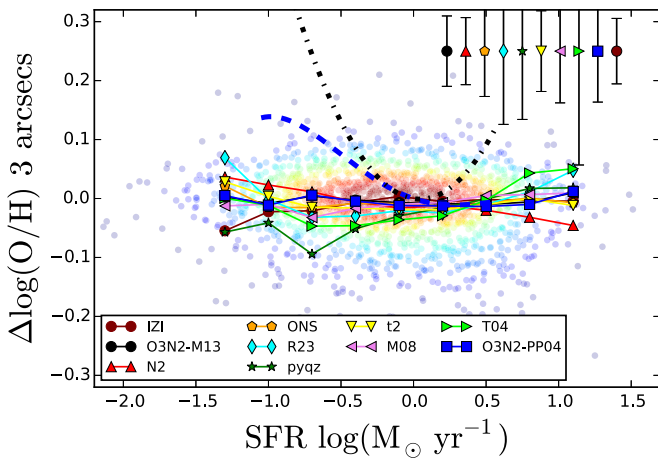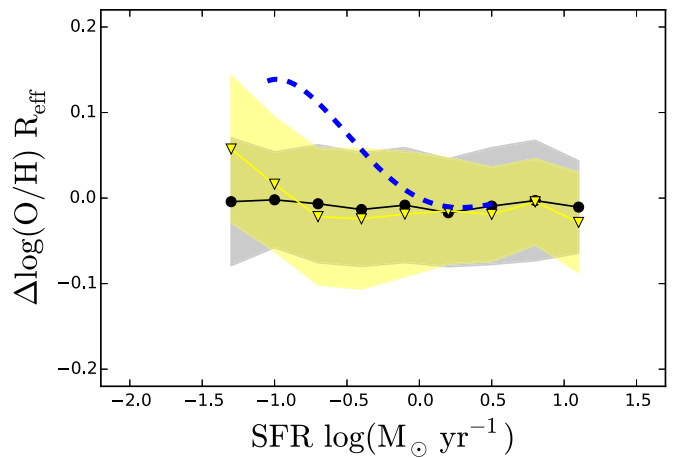

Figure 7. Same as Figure 3, but with the derived MZR for all the metallicity calibrators and their corresponding residuals measured in a galactocentric aperture with a 3 arcsec diameter.

Figure 9. MZR residuals against the SFR using two calibrators. The gray and yellow points and lines represent the median residuals for the O3N2-M13 and t2 indicators, respectively. The shaded regions represent the area covered by the standard deviation. As in Figure 3, the blue dotted line represents the Mannucci et al. (2010) relation.

where the median residuals are almost constant. This comparison suggests that even if there is a secondary relation of the MZR with the SFR, it is weaker than those reported previously in the literature. It also indicates that this possible secondary relation may not be as robust as the MZR itself since it does depend on the selected metallicity calibrator.

Except for the lowest sSFR bin, the MZR residuals are constant regardless of the metallicity calibrator (see, Figure 4). When we compare the residuals of the MZR with the sSFR, we are comparing quantities that in principle should not have any relation with the stellar mass, since both are normalized to this quantity. This in turn indicates that a secondary relation observed between these two quantities would be a strong indication of the actual impact of the SFR on the metal content of galaxies. Then, the result we observed in Figure 4 would be a very strong indication that metals do not seem to depend strongly on the SFR.

In a recent article, Salim et al. (2014) found that the observed metallicity anti-correlates with the sSFR for SDSS galaxies located in the star formation main-sequence. To account for the impact of the stellar mass, they compared the metallicity and the sSFR for different mass bins. They stressed that the overall

Figure 8. Same as Figure 4, but with the derived MZR for all the metallicity calibrators and their corresponding residuals measured in a galactocentric aperture with a 3 arcsec diameter.

the t2 calibrator the distribution of metallicity residuals includes those expected by Mannucci et al. (2010), although not for the entire SFR range. At the lowest SFR, the expected relation from Mannucci et al. (2010) is not able to reproduce the t2 residual distributions. The same is true for O3N2-M13,

scatter from their observed mass–metallicity–SFR relation does not significantly reduce the scatter observed in their MZR. Our results agree qualitatively with the main conclusions from this study. We observe, at best, a weak dependence of the residuals on the metallicity (in other words, when we remove the stellar mass dependency on the metallicity) against the sSFR for the entire set of galaxies, regardless of the metallicity calibrator. Once we divide our sample into stellar mass bins, we find trends for the residuals of the MZR with the SFR and sSFR (see Figures 5 and 6). However, these trends depend on the selected metallicity calibrator. A possible reason for the difference in these two studies is that we compare the residuals of the MZR instead of only the metallicity to the SFR. As we explain above, this ensures that we are comparing two quantities that are not heavily dependent on the stellar mass. In conclusion, we suggest that previously observed trends between the metallicity and the sSFR could be induced by the discrimination of galaxies into mass bins, as well as a lack of proper subtraction of the dependence of the stellar mass from the metallicity.

The spatially resolved data allowed us to study (in Section 4.2) the metallicity measured by the emission-line fluxes integrated in a 3 arcsec aperture centered in the optical nucleus of our sample of galaxies. This emulates the metallicity data from a single-fiber spectroscopy, such as the SDSS spectroscopic data. We performed the same analysis done at the effective radius (see Figures 7 and 8). The trend we observed between the MZR residuals and the SFR using this 3 arcsec aperture was quite similar to those observed at the effective radius. This suggests that the lack (or weak) relation of the MZR and the SFR is independent of the spatial scale. This result also is very robust for different metallicity calibrators. Our data are also in agreement with recent results showing a lack or weak secondary relation of the MZR with the SFR for single-fiber aperture data. Using a single metallicity calibrator, Kashino et al. (2016) showed that they were not able to reproduce the secondary relation between the SFR and the MZR proposed by Mannucci et al. (2010). Ironically enough, as noted in their conclusions, the lack of a secondary relation was consistent with its existence. They claim that their metallicity calibrator is not sensitive to metallicity dilution or enhancement of the SFR due to metal-poor gas infall, therefore even if there was a secondary relation they were expected not to observe it. On the other hand, Telford et al. (2016) explored systematic effects of the secondary relation between the MZR and the SFR. They found a weaker secondary relation in comparison to the one presented by Mannucci et al. (2010). Along with these studies, our results show that even at the central region, the assumed secondary relation with the SFR or the sSFR, if it exists, is much weaker than previously claimed.

The existence or lack thereof of an observational relation between these three parameters has a significant impact on how we understand the evolution and structure of galaxies in the universe. Analytical and semi-analytical models, as well as numerical simulations, have explained this triple relation by invoking an interplay between global metal-poor gas inflow and outflows that remove enriched material far out of the reach of the potential well of the galaxy (e.g., Finlator 2016, and references therein). In a parallel work, we examine this possible secondary relation using the CALIFA spatially resolved data set (Sánchez et al. 2017). We find results similar to those presented in this study. Indeed, there is no clear trend or statistically significant reduction of the scatter of the MZR

when introducing a secondary dependence either with the SFR or the sSFR. The fact that we could not find a clear secondary relation neither at the central region nor at the effective radius indicates that the process responsible for the MZR seems to be scale-independent. We identify these results using the enrichment of the interstellar medium, which must be dependent on local processes, with a strong dependence on the local star formation history, and local downsizing. Indeed, Rosales-Ortega et al. (2012) found a local MZR analogical relation between the surface mass density (Σ_*) and local metallicity. At low Σ_* the local metallicity increases, similar to the MZR for $\log(M_*/M_\odot) < 10$, indicating that metal enrichment and star formation are still occurring. At larger Σ_* (or M_*), both local and global metallicities reach a constant metallicity, suggesting that in those regions (or galaxies) star formation has ceased. Following this relation, it is also possible to reproduce the observed metallicity gradients in disk galaxies using the Σ_* radial distributions (Barrera-Ballesteros et al. 2016). In conclusion, we suggest that global stellar MZR is primarily a consequence of the metal enrichment by the stellar population at local scales. Although we cannot completely rule out a dependency of the metallicity with the SFR, we find that if it exists it is much weaker than previously reported.

6. Conclusions

We study the integrated stellar MZR for more than 1700 galaxies included in the ongoing SDSS-IV MaNGA survey. The wealth of this integral field spectroscopic data allows us to determine the metallicity at a fixed physical scale ($R_{\rm eff}$) using a set of 10 calibrators covering a broad range of methods from empirical, to mixed, to pure photoionization models. We confirm for all calibrators the reported trend of the MZR using large samples of single-fiber spectroscopic data (e.g., Tremonti et al. 2004; Mannucci et al. 2010), as well as those reported using integral field spectroscopy (e.g., Rosales-Ortega et al. 2012; Sánchez et al. 2014; Barrera-Ballesteros et al. 2016), albeit after scaling factors (e.g., Kewley & Ellison 2008). Furthermore, we find that direct-method and t_2-based calibrators show a MZR with smaller dispersion with respect to mixed and pure photoionization calibrators.

We also explore a possible secondary relation of the MZR with the star formation rate (SFR), as well as with the specific SFR (sSFR). We find that the residuals of the MZR do not show an evident correlation with SFR nr with the sSFR, regardless of the abundance calibrators used in this study. A further linear fitting of these residuals with the SFR or sSFR does not reduce the observed scatter. Moreover, we note that the dispersion of these residuals is of the order of magnitude as the errors of the adopted calibrators in most of the cases (e.g., Marino et al. 2013); therefore it is not expected to have any possible secondary relation in any case. The above results are also valid when considering the metallicity found using fluxes integrated in a 3 arcsec aperture centered in their optical nuclei.

This work is strong evidence supporting the notion of a lack of a secondary relation of the SFR with the MZR. Our results suggest that chemical enrichment in galaxies mainly occurs at local scales as proposed by Rosales-Ortega et al. (2012), Sánchez et al. (2014); this was confirmed recently using data from the MaNGA survey (Barrera-Ballesteros et al. 2016). This in turn also suggests that large-scale outflows do not appear to be the primary mechanism for enriching the ISM, whereas inflows seem to regulate the SFR (Lilly et al. 2013).

Finally, we note that a local/global SFR–stellar mass sequence (SFMS, e.g., Sánchez et al. 2013; Cano-Díaz et al. 2016) implies that a possible secondary relation of the MZR with the SFR would just be a re-scaling of the stellar mass-axis, rather than a reduction in the scatter of the MZR.

References

Baldwin, J. A., Phillips, M. M., & Terlevich, R. 1981, PASP, 93, 5
Barrera-Ballesteros, J. K., Heckman, T. M., Zhu, G. B., et al. 2016, MNRAS, 463, 2513
Blanc, G. A., Kewley, L., Vogt, F. P. A., & Dopita, M. A. 2015, ApJ, 798, 99
Brinchmann, J., Charlot, S., White, S. D. M., et al. 2004, MNRAS, 351, 1151
Bundy, K., Bershady, M. A., Law, D. R., et al. 2015, ApJ, 798, 7
Cano-Díaz, M., Sánchez, S. F., Zibetti, S., et al. 2016, ApJL, 821, L26
Catalán-Torrecilla, C., Gil de Paz, A., Castillo-Morales, A., et al. 2015, A&A, 584, A87
Cid Fernandes, R., Stasińska, G., Mateus, A., & Vale Asari, N. 2011, MNRAS, 413, 1687
Dopita, M. A., Sutherland, R. S., Nicholls, D. C., Kewley, L. J., & Vogt, F. P. A. 2013, ApJS, 208, 10
Drory, N., MacDonald, N., Bershady, M. A., et al. 2015, AJ, 149, 77
Ellison, S. L., Patton, D. R., Simard, L., & McConnachie, A. W. 2008, ApJL, 672, L107
Finlator, K. 2016, arXiv:1612.00802
Gomes, J. M., Papaderos, P., Vilchez, J. M., et al. 2016, A&A, 586, A22
Gunn, J. E., Siegmund, W. A., Mannery, E. J., et al. 2006, AJ, 131, 2332
Hughes, T. M., Cortese, L., Boselli, A., Gavazzi, G., & Davies, J. I. 2013, A&A, 550, A115
Iglesias-Páramo, J., Vilchez, J. M., Galbany, L., et al. 2013, A&A, 553, L7
Iglesias-Páramo, J., Vilchez, J. M., Rosales-Ortega, F. F., et al. 2016, ApJ, 826, 71
Kashino, D., Renzini, A., Silverman, J. D., & Daddi, E. 2016, ApJL, 823, L24
Kauffmann, G., Heckman, T. M., Tremonti, C., et al. 2003, MNRAS, 346, 1055
Kennicutt, Jr. R. C. 1998, ApJ, 498, 541
Kewley, L. J., & Ellison, S. L. 2008, ApJ, 681, 1183
Lara-López, M. A., Cepa, J., Bongiovanni, A., et al. 2010, A&A, 521, L53
Law, D. R., Cherinka, B., Yan, R., et al. 2016, AJ, 152, 83
Lilly, S. J., Carollo, C. M., Pipino, A., Renzini, A., & Peng, Y. 2013, ApJ, 772, 119
Maiolino, R., Nagao, T., Grazian, A., et al. 2008, A&A, 488, 463
Mannucci, F., Cresci, G., Maiolino, R., Marconi, A., & Gnerucci, A. 2010, MNRAS, 408, 2115
Marino, R. A., Rosales-Ortega, F. F., Sánchez, F. S., et al. 2013, A&A, 559, A114
Moran, S. M., Hecman, T. M., Kauffmann, G., et al. 2012, ApJ, 745, 66
Moustakas, J., Zaritsky, D., Brown, M., et al. 2011, arXiv:1112.3300
Peña-Guerrero, M. A., Peimbert, A., & Peimbert, M. 2012, ApJL, 756, L14
Pettini, M., & Pagel, B. E. J. 2004, MNRAS, 348, L59
Pilyugin, L. S., Vílchez, J. M., & Thuan, T. X. 2010, ApJ, 720, 1738
Rosales-Ortega, F. F. 2010, PhD thesis, Univ. Cambridge
Rosales-Ortega, F. F., Sánchez, S. F., Iglesias-Páramo, J., et al. 2012, ApJL, 756, L31
Salim, S., Lee, J. C., Ly, C., et al. 2014, ApJ, 797, 126
Sánchez, S., Sánchez-Menguiano, L., Marino, R., et al. 2015a, Galax, 3, 164
Sánchez, S. F., Barrera-Ballesteros, J. K., Sánchez-Menguiano, L., et al. 2017, MNRAS, in press
Sánchez, S. F., Kennicutt, R. C., Gil de Paz, A., et al. 2012, A&A, 538, A8
Sánchez, S. F., Pérez, E., Sánchez-Blázquez, P., et al. 2015b, RMxAA, submitted (arXiv:1509.08552)
Sánchez, S. F., Pérez, E., Sánchez-Blázquez, P., et al. 2016, RMxAA, in press (arXiv:1602.01830)
Sánchez, S. F., Rosales-Ortega, F. F., Ingesias-Paramo, J., et al. 2014, A&A, 563, A49
Sánchez, S. F., Rosales-Ortega, F. F., Jungwiert, B., et al. 2013, A&A, 554, A58
Sánchez-Menguiano, L., Sánchez, S. F., Pérez, I., et al. 2016, A&A, 587, A70
Smee, S. A., Gunn, J. E., Uomoto, A., et al. 2013, AJ, 146, 32
Telford, O. G., Dalcanton, J. J., Skillman, E. D., & Conroy, C. 2016, ApJ, 827, 35
Tremonti, C. A., Heckman, T. M., Kauffmann, G., et al. 2004, ApJ, 613, 898
Vila-Costas, M. B., & Edmunds, M. G. 1992, MNRAS, 259, 121
Wake, D. 2016, AAS meeting, 27, 334.01
Yan, R., Tremonti, C., Bershady, M. A., et al. 2016, AJ, 151, 8